Atmos. Meas. Tech. Discuss., 7, 9137–9172, 2014
www.atmos-meas-tech-discuss.net/7/9137/2014/
doi:10.5194/amtd-7-9137-2014

Atmospheric Measurement Techniques Discussions

BINARY: an optical freezing array for assessing temperature and time dependence of heterogeneous ice nucleation

C. Budke and T. Koop

Faculty of Chemistry, Bielefeld University, Universitätsstraße 25, 33615 Bielefeld, Germany

Received: 23 August 2014 – Accepted: 25 August 2014 – Published: 10 September 2014

Correspondence to: T. Koop (thomas.koop@uni-bielefeld.de)

Published by Copernicus Publications on behalf of the European Geosciences Union.

Abstract

A new optical freezing array for the study of heterogeneous ice nucleation in microliter-sized droplets is introduced, tested and applied to the study of immersion freezing in aqueous Snomax® suspensions. In the Bielefeld Ice Nucleation ARraY (BINARY) ice nucleation can be studied simultaneously in 36 droplets at temperatures down to −40 °C (233 K) and at cooling rates between 0.1 K min^{-1} and 10 K min^{-1}. The droplets are separated from each other in individual compartments, thus preventing a Wegener–Bergeron–Findeisen type water vapor transfer between droplets as well as avoiding the seeding of neighboring droplets by formation and surface growth of frost halos. Analysis of freezing and melting occurs via an automated real time image analysis of the optical brightness of each individual droplet. As an application ice nucleation in water droplets containing Snomax® at concentrations from 1 ng mL^{-1} to 1 mg mL^{-1} was investigated. Using different cooling rates a minute time dependence of ice nucleation induced by Class A and Class C ice nucleators contained in Snomax® was detected. For the Class A IN a very strong increase of the heterogeneous ice nucleation rate coefficient with decreasing temperature of $\lambda \equiv -\mathrm{d}\ln(j_{\mathrm{het}})/\mathrm{d}T = 8.7\,\mathrm{K}^{-1}$ was observed emphasizing the capability of the BINARY device. This value is larger than those of other types of IN reported in the literature, suggesting that the BINARY setup is suitable for quantifying time dependence for most other IN of atmospheric interest, making it a useful tool for future investigations.

1 Introduction

Atmospheric ice nucleation is one of the key steps in high altitude cloud formation and also for triggering precipitation in mixed-phase clouds (Pruppacher and Klett, 1997; Lamb and Verlinde, 2011). Ice particles can be formed via homogeneous ice nucleation in liquid aerosol and water droplets (Koop et al., 2000), or via heterogeneous ice nucleation triggered by pre-existing ice nucleators (IN) (Cziczo and Froyd, 2014). Both

AMTD
7, 9137–9172, 2014

homogeneous as well as heterogeneous ice nucleation processes do occur and various approaches of parameterizing them in atmospheric models have been described. One strategy for improving the description of ice nucleation in cloud models is the elucidation of the responsible mechanisms and their physical dependencies in laboratory experiments. For example, such laboratory data can then serve as a basis for physically consistent parameterizations for heterogeneous ice nucleation that can be incorporated into process models (Hoose and Möhler, 2012). In mixed-phase clouds heterogeneous immersion mode freezing is thought to be a relevant process (Pruppacher and Klett, 1997; Lohmann and Diehl, 2006). Representing immersion freezing, however, has been particularly difficult, in part because of the way in which time-dependence of ice nucleation is represented in current models (Ervens and Feingold, 2013). It is well accepted that homogeneous ice nucleation is a time-dependent stochastic process which can be described by the formation of an ice embryo with critical size, whose probability to form increases with time (Pruppacher and Klett, 1997; Murray et al., 2010; Riechers et al., 2013). There is, however, an ongoing debate on whether heterogeneous ice nucleation in the immersion mode is only temperature dependent (i.e., a singular process) or both temperature and time dependent (i.e., a stochastic process) (Vali, 2014). In a stochastic process, the probability for the occurrence of a nucleation event increases exponentially with time at a rate that depends on temperature (e.g., Bigg, 1953; Vonnegut and Baldwin, 1984; Pruppacher and Klett, 1997; Vali, 1994, 2014). In contrast, in a singular process no such time dependence of ice nucleation exists, because the probability for ice nucleation switches instantaneously from zero to one at a deterministic temperature that depends on the IN (e.g., Vali and Stansbury, 1966). Moreover, another so-called modified singular process has been proposed that describes the overall process as temperature dependent with a small stochastic variation around the deterministic temperature (Vali, 2008).

Several studies have employed experimental data and model calculations to show very little time dependence thus justifying the use of the time-independent singular approach (Kulkarni et al., 2012; Welti et al., 2012; Wright and Petters, 2013). But it has

AMTD
7, 9137–9172, 2014

been suggested more recently that any existing small time dependence may not be neglected, if a more accurate description of heterogeneous nucleation is to be achieved in models. One drawback from which many experimental techniques suffer is the fact that cooling rates or the rates by which the supersaturation changes can be varied over a small range only, thus limiting their sensitivity to distinguish between the different approaches (see, e.g., the discussion in Niedermeier et al., 2010; Lüönd et al., 2010).

Several instrumental techniques are available for the determination of the above mentioned processes (Murray et al., 2012; Hoose and Möhler, 2012). One of the commonly used methods is based on an early description of a drop-freezer apparatus developed by Vali (Vali and Stansbury, 1966; Vali, 1971). In the original setup, microliter-sized droplets are pipetted onto a substrate that is placed on a thermoelectric cooler. The droplets are separated by about 1 cm from each other, but no other precautions are taken to avoid a Wegener–Bergeron–Findeisen type process, i.e. the growth of frozen droplets at the expense of remaining supercooled liquid ones by water vapor transfer. In addition, the latent heat release during freezing may cause the formation of frost halos that subsequently may grow and expand around the frozen droplets by Wegener–Bergeron–Findeisen type water vapor transfer (Jung et al., 2012; Welz, 2013). This frost halo growth bears the risk of seeding neighboring droplets thus biasing the recorded ice nucleation temperatures (Jung et al., 2012; Welz, 2013). To circumvent these problems and to minimize evaporation, droplets are often covered with an oil film (Bigg, 1953; Hoffer, 1961; Murray et al., 2011; Pummer et al., 2012; Wright and Petters, 2013). But the use of such emulsion-type samples may lead to alternative problems because some IN such as pollen or fungal spores may have an affinity to the hydrophobic phase. When a part of the dispersed IN material is lost to the oil phase an overestimation of IN concentration may result, leading to an underestimation of IN activity. Another uncertainty arises if surfactants are used for the stabilization of emulsions, because surfactants may also influence the investigated IN at the water/oil interface (Pummer et al., 2012), particularly when the IN reside predominantly at the droplet surface.

AMTD
7, 9137–9172, 2014

A very recent instrument development of Stopelli et al. (2014) uses sealable tubes to prevent evaporation and cross-contamination of the investigated suspensions. The device bears an additional advantage over previous tube-base ice nucleation devices (e.g., Barlow and Haymet, 1995; Heneghan et al., 2002) in that it allows simultaneous investigation of multiple samples rather than focusing on numerous freeze–thaw repeats of a limited number of samples. Another improvement is the nature of the substrate on which the droplets are positioned. In the original drop-freezer water droplets were pipetted onto an oil-covered sheet of aluminum foil (Vali and Stansbury, 1966). More recent techniques make use of advanced chemical approaches to hydrophobize glass or quartz substrates by a self-assembled monolayer (e.g., using a halogenated silane), which does not affect the mechanical or thermal properties of the substrate (Koop et al., 1998; Salcedo et al., 2000; Knopf and Lopez, 2009; Murray et al., 2010; Iannone et al., 2011).

Some of the devices introduced in the past for the analysis of heterogeneous ice nucleation employ rather large sample volumes (tens to hundreds of microliters) in order to be able to further analyze the ice nucleating substances, for long term IN sample storage and an associated investigation of ageing effects, or to ease the detection of freezing (Barlow and Haymet, 1995; Attard et al., 2012; Stopelli et al., 2014). Others have focused on rather small (often emulsified) samples (picoliters to nanoliters) in order to minimize or exclude the unwanted effects of ice nucleating impurities contained in the water for preparing the suspensions under scrutiny (Koop and Zobrist, 2009; Murray et al., 2010, 2011; Pummer et al., 2012; Wright and Petters, 2013; Atkinson et al., 2013). Herein we use intermediate volume samples of 1 microliter which are easy to prepare and are not subject to concentration uncertainties owing to water evaporation during sample preparation and storage. For such volumes heterogeneous ice nucleation from impurities contained in the "pure" water usually occurs at temperatures below −20 °C (253 K). Therefore, such samples are applicable for ice nucleation studies over the important temperature range of mixed phase clouds between −20 °C (253 K) and 0 °C (273 K).

AMTD
7, 9137–9172, 2014

In the following, we introduce a new droplet freezing assay, in which the separation of the investigated water droplets is accomplished by a polymer spacer. This spacer encloses each of a total of 36 microliter-sized droplets individually without direct contact to any of them. Moreover, we have developed an automated system for analyzing the freezing temperature of each drop. Finally, the device allows for an accurate determination of ice nucleation temperatures over a large range of cooling rates from 0.1 to 10 K min^{-1}. We chose Snomax®, a commercially available ice inducer used in snow cannons, as a test substance for the investigation of heterogeneous ice nucleation and an assessment of its temperature and time dependence.

2 Experimental Setup

The optical freezing apparatus introduced here, which we term BINARY (Bielefeld Ice Nucleation ARraY), consists of a 6×6 array of individual microliter-sized droplets (normally 1 µL per droplet, but 0.5–5 µL work too) positioned on a thin hydrophobic glass slide (Fig. 1a). The droplets are separated from each other by a soft polydimethylsiloxane (PDMS) spacer and the resulting compartments are sealed at the top with another glass slide (Fig. 1b). The PDMS spacer is fabricated from a 10 : 1 mixture of base polymer to curing agent (Sylgard® 184, Dow Corning) pored onto a mold made from aluminum that was custom designed to represent the compartment array.

The droplet separation into individual compartments prevents a Wegener–Bergeron–Findeisen process, in which frozen droplets grow at the expense of unfrozen supercooled liquid droplets due to the vapor pressure difference between ice and supercooled liquid water (Murphy and Koop, 2005). This process poses a particular problem to droplet arrays operated at small cooling rates or employing stepwise cooling and has been noted frequently to influence and corrupt ice nucleation measurements (Welz, 2013; Stopelli et al., 2014; O'Sullivan et al., 2014). In addition, the probability of heterogeneous ice nucleation at the lower glass surface is minimized by the hydrophobicity of

AMTD
7, 9137–9172, 2014

the glass and the effect of ice nucleating impurities in water is reduced by using freshly double-distilled water.

The sample array is placed onto a Peltier cooling stage (Fig. 1c), which is part of a commercially available cooling stage system (Linkam LTS120). Good thermal contact between the Peltier stage and the lower glass surface of the sample array is achieved by pressing the upper glass slide towards the stage with 4 fixing screws, one at each corner. When the Peltier stage is connected to a heat sink bath at 5 °C (278 K), the sample array can be cooled to −40 °C (233 K) at cooling rates between 0.1 and 10 K min^{-1}. The cover of the cooling stage was modified to consist of a larger opening sealed with a thin glass window such that the resulting larger field of view of 40 mm × 40 mm allowed for the simultaneous observation of all droplets of the sample array. In addition, small arrays of cold-light white LEDs were fixed to the top of the cooling chamber to yield the proper contrast for identifying the phase state of the droplets, see below. Finally, purging of dry N_2 gas into the chamber as well as onto the top window prevents dew and frost formation from laboratory humidity during cooling.

A LabVIEW™ virtual instrument is used to control the temperature of the Peltier stage and to analyze in real time the digital images obtained by a CCD camera (QImaging MicroPublisher 5.0 RTV). The images are recorded and analyzed at a frequency that depends upon the experimental cooling rate: three successive images are analyzed per 0.1 K temperature interval, i.e. one image every 0.0$\bar{3}$ K. For example, the corresponding time interval $|\Delta t_{j-1,j}|$ between successive images $j-1$ and j at a cooling rate of 1 K min^{-1} and 5 K min^{-1} are 2 and 0.4 s, respectively. Moreover, every third image is stored in digital format allowing for later re-examination or re-analysis. These images have a temperature resolution of 0.1 K.

Ice nucleation is determined optically based on the change in droplet brightness when the initially transparent liquid droplets become opaque upon freezing (see Fig. 2a and the movie of this experiment available in the Supplement). This change in brightness is maximized by illuminating the droplets by LEDs at a low sideway angle from the top (see Fig. 1c) and also by the reflective top surface of the Peltier stage. The

AMTD
7, 9137–9172, 2014

8-bit mean gray value, gv, (ranging from gv = 0 for black to gv = 255 for white) is determined for each compartment/droplet i in every image j. The difference in gv between successive images and, hence, temperatures $\Delta gv_{i,j}(T) = gv_{i,j} - gv_{i,j-1}$ is then used to determine droplet freezing and melting.

Figure 2 shows an example experiment of water droplets containing Snomax® at a concentration of 1×10^{-1} µg drop^{-1}. In panel (a) three images are shown of the entire array during cooling. At −3.5 °C (269.6 K) all droplets are still liquid as recognized by their dark appearance and at −5.5 °C (267.6 K) all droplets are frozen and bright. At the intermediate −4.5 °C (268.6 K) some bright spots indicate frozen or currently freezing droplets. In panel (b) a more detailed analysis is exemplified for the droplet shown in the yellow box in panel (a). The droplet is first cooled and subsequently reheated at rates of 1 K min^{-1}. The mean gray value gv for the droplet is determined from all pixels contained in the yellow box. In the beginning the gray value increases only slightly during cooling, due to condensation of water vapor contained in the compartment onto the bottom glass plate. Ice nucleation in the droplet occurs at −3.9 °C (269.2 K) resulting in a steep increase of the gray value from about 30 to nearly 70 at −4.2 °C (269.0 K) in the few subsequent images. While the largest gray value change Δgv between two consecutive images is about 10 at a temperature slightly below −4 °C (269 K, see Fig. 2c for comparison), nucleation and freezing is detected already a few images before. We set a threshold value of $\Delta gv > 1$ for the automatic attribution of ice nucleation, since all other Δgv values during the entire cooling procedure are significantly smaller than 1 at a typical noise level of $\Delta gv \lesssim \pm 0.2$ (Fig. 2c).

Following droplet freezing the previously condensed liquid water then evaporates and freezes onto the frozen droplet leading to the formation of a frost halo and a slow decrease in gv to about 62 in this particular case (Fig. 2b). Upon heating this value more slowly decreases further since the polycrystalline ice slowly recrystallizes thus reducing the amount of ice facets capable of scattering of light. Finally, gv increases just before reaching the melting point due to formation of liquid water films in the grain boundaries of the frozen droplet, thus light is reflected slightly more efficiently. The

AMTD
7, 9137–9172, 2014

onset of melting at 0 °C (273 K), most easily observed at the halo, finally results in a decrease of gv and hence a negative peak in Δgv, see Fig. 2c. We set a threshold value of $\Delta gv < -1$ for automatic attribution of melting. We note that at a heating rate of 1 K min^{-1} the melting of the entire droplet is complete at about 2 °C (275 K).

The analysis described in Fig. 2 is performed automatically for all droplets of a particular array. The nucleation temperatures thus obtained for each droplet undergo a correction according to a temperature calibration that is outlined in the next section.

3 Temperature calibration

The experiment discussed in the previous section was performed at a constant cooling rate of 1 K min^{-1}. Investigation of time dependence of heterogeneous ice nucleation in such constant cooling rate experiments requires performing several experiments at different cooling rates (see e.g. Herbert et al., 2014). Therefore, we conducted a comprehensive calibration exercise that accounts for variable cooling rates in BINARY. The calibration was performed using five reference phase transitions in the temperature range of interest from −37 °C to 0 °C (236 to 273 K, see Table 1 and Fig. 8 in the Appendix) and for heating rates from 0.1 to 10 K min^{-1}. The rate calibration was conducted in the heating mode because superheating is usually negligible while even minor supercooling would bias a calibration in cooling mode (Sarge et al., 2000; Della Gatta et al., 2006). For the solid-liquid phase transition of tridecane the rate dependence of cooling vs. heating was investigated. Although crystal nucleation temperatures of tridecane droplets in the size range from 0.1 to 1.5 µL scattered significantly more (by about 0.8 K between the 25th to 75th percentiles) than observed for the melting temperatures during calibration (about 0.2 K) the observed dependence of nucleation temperatures with increasing cooling rate was similar to that of the melting temperatures with increasing heating rate (∼ 0.02 and ∼ 0.05 min, respectively).

For the calibration procedure the reference substances were sprayed onto the hydrophobic glass slide resulting in droplets of about 0.05 µL (∼ 0.6 mm) thus ensuring

AMTD
7, 9137–9172, 2014

the detection of the onset of the phase transition. The threshold value for automatic detection of the phase transitions was adjusted accordingly, in particular for the solid-solid phase transitions which involve smaller Δgv values. The phase transition temperatures obtained were analyzed by separating the absolute temperature offset of the sample array at zero rate from its rate dependence as recommended for the calibration of thermal devices (Sarge et al., 2000; Della Gatta et al., 2006; Riechers et al., 2013). Figure 3a shows the difference between the experimentally observed temperatures T_{exp} and the literature values T_{lit} as a function of heating rate. Points represent the median values and error bars indicate the 25th and 75th percentiles of the data from different compartments and multiple cooling/heating cycles. Using a linear fit to each individual reference substance's data set the absolute temperature deviation at zero rate is associated to the intercept and the rate dependence is represented by the slope. The results of this procedure are shown in Fig. 3b as a function of T_{exp} with intercept values (red diamonds and left axis) and slope values (green triangles and right axis). Accordingly, the absolute temperature deviation at zero rate is well represented by a linear fit (red line) and the rate dependence by a second-order polynomial (green line). The remaining uncertainty after calibration, which is the absolute difference between the calibrated temperatures T_{cal} and the literature values T_{lit}, is shown in Fig. 3c. The squares represent the median values and the error bars the 25th and 75th percentiles of each substance. We note that $|T_{cal} - T_{lit}|$ is smaller than 0.3 K for 97 % of all individual data points, indicating the quality of the calibration procedure.

4 Results

We put the new BINARY setup to the test using Snomax® as a well-studied ice-nucleating substance. Snomax® is a commercial product containing freeze-dried non-viable bacterial cells from *Pseudomonas syringae*, which are known to be active IN at rather high temperature. First, experiments with droplets of 1 µL volume were investigated at a cooling rate of 1 K min^{-1}. Snomax® concentrations were varied over 6

AMTD
7, 9137–9172, 2014

orders of magnitude between 1 ng mL^{-1} and 1 mg mL^{-1} corresponding to a total mass between 1 pg per droplet and 1 µg per droplet, respectively. Usually, 108 droplet freezing events (from 3 × 36 droplets) were analyzed at each concentration. The results of these experiments are shown in Fig. 4 by plotting $n_m(T)$, the cumulative number of ice nucleators per µg of Snomax®, as a function of temperature. $n_m(T)$ can be obtained from the raw data by analyzing the frozen fraction f_{ice} from the cumulative number of frozen droplets $n_{ice}(T)$ and the total number of droplets n_{tot} of a particular Snomax® concentration:

$$f_{ice}(T) = \frac{n_{ice}(T)}{n_{tot}} = 1 - e^{-K(T)V}. \quad (1)$$

From Eq. (1) the cumulative ice nucleator concentration $K(T)$ can be deduced, which is typically referred to as the active site number density per unit droplet volume V. Because we know the mass concentration C_m of Snomax® and the volume V of the droplets, $K(T)$ can be converted into the active site density per unit mass $n_m(T)$:

$$n_m(T) = \frac{K(T)}{C_m} \left[= n_s(T) \cdot S' = n_n(T) \cdot N' \right]. \quad (2)$$

Likewise the active site density per unit surface area $n_s(T)$ or per particle number $n_n(T)$ can be deduced, if the specific surface area S', i.e. the surface area per sample mass, or the specific particle number N', i.e. the number of particles per sample mass, respectively, are known from independent analysis (Fletcher, 1969; Connolly et al., 2009; Murray et al., 2012; Niemand et al., 2012).

Figure 4 shows two particularly strong increases in $n_m(T)$, one at about −3.5 °C (269.6 K) ±0.5 K and one at −8.5 °C (264.6 K) ±0.5 K, indicating the presence of two distinct ice nucleators with different activation temperatures. It is already known that different types of IN or aggregates of IN are responsible for ice nucleation induced by *Pseudomonas* and other ice nucleating bacteria in different temperature ranges

AMTD
7, 9137–9172, 2014

(Yankofsky et al., 1981; Turner et al., 1990; Hartmann et al., 2013). For example, Turner et al. (1990) identified three classes of IN on the basis of the temperature at which they triggered ice nucleation: Class A at high temperature ($\gtrsim -4\,^{\circ}\mathrm{C} \simeq 269\,\mathrm{K}$), Class B in the intermediate range (approx. -5 to $-7\,^{\circ}\mathrm{C} \simeq 268$ to $266\,\mathrm{K}$), and Class C at lower temperature ($\lesssim -8\,^{\circ}\mathrm{C} \simeq 265\,\mathrm{K}$). According to this definition the data shown in Fig. 4 suggest that our sample contained Class A and Class C ice nucleating proteins or protein complexes.

The two plateaus at temperatures just below each increase of $n_{\mathrm{m}}(T)$ in Fig. 4 arise when no IN active at these temperatures are present in the investigated suspensions. The $n_{\mathrm{m}}(T)$ values of the plateaus differ by about 3 orders of magnitude, from which we infer that the Class A and Class C Snomax® IN occur at a number ratio of about 1 to 1000 in our samples. The active site densities per cell $n_{\mathrm{n}}(T)$ shown in Fig. 4 on the right axis were calculated using the specific particle number of cells in Snomax® of $N' = 1.4 \times 10^{9}\,\mathrm{mg}^{-1}$ determined by Wex et al. (2014) using multiple instruments including the BINARY setup presented here.

Previously, Turner et al. (1990) identified Snomax® to contain IN of Class A and Class B, but none of Class C. This difference to our study may result from varied growth or storage conditions of different Snomax® samples and is in line with their proposal that Class C IN can develop into Class B (and subsequently into Class A) IN by accumulation of larger ice nucleating protein complexes in the cell membranes. In fact, our sample may contain also Class B IN, but the low number of freezing events in the corresponding temperature range of -5 to $-7\,^{\circ}\mathrm{C}$ (268 to 266 K) indicates that there are less IN of Class B than there are of Class A, the latter of which trigger ice nucleation already at higher temperature. As mentioned above, in our sample the more active but less abundant Class A ice nucleators induce freezing at about $-3.5\,^{\circ}\mathrm{C}$ (269.6 K) $\pm 0.5\,\mathrm{K}$ and they dominate the freezing of droplets at a Snomax® concentration of $1 \times 10^{-1}\,\mu\mathrm{g\,drop}^{-1}$. The less active but more abundant IN of Class C nucleate ice at about $-8.5\,^{\circ}\mathrm{C}$ (264.6 K) $\pm 0.5\,\mathrm{K}$. At a Snomax® concentration of $1 \times 10^{-5}\,\mu\mathrm{g\,drop}^{-1}$ almost all droplets contain such IN of Class C, but practically none of Class A anymore.

AMTD
7, 9137–9172, 2014

The analysis shown in Fig. 4 is based on the singular approach which assumes that the results are independent of time and, hence, cooling rate. With the new BINARY setup we were able to challenge this assumption by performing experiments at different cooling rates in the range from 0.1 to 10 K min^{-1}. In particular the cooling rate dependence of the two IN Classes discussed above was investigated. Figure 5 shows a decrease in the median ice nucleation temperature $T_{f,50}$ with increasing cooling rate for both Classes of IN. The $T_{f,50}$ values are represented by filled symbols with error bars indicating the 25th and 75th percentiles. In the following analysis temperature was divided into equally spaced intervals $\Delta T = T_1 - T_2 = 0.1$ K and all data were binned into these temperature intervals with interval temperature $T = T_1 - 0.5 \cdot \Delta T$. They are shown as open symbols with symbol size corresponding to the number of ice nucleation events $\Delta n_{ice}(T) = n_{liq}(T_1) - n_{liq}(T_2)$, i.e. more nucleation events lead to larger symbols. At the indicated concentrations the difference between the $T_{f,50}$ values at 10 and at 0.1 K min^{-1} is about 0.6 K for both Classes of IN (0.55 K for Class A and 0.64 K for Class C). These values are rather small but they are significantly larger than our temperature uncertainty, implying that we were able to detect a rather minute time dependence for each of the two IN Classes.

The above analysis suggests a time dependence of Snomax® induced ice nucleation. Therefore, we may expect to see deviations in the active site density obtained at different cooling rates. Figure 6a shows $n_m(T)$ at the two investigated Snomax® concentrations at different cooling rates. Clearly, there is a systematic trend towards lower $n_m(T)$ with larger cooling rate, i.e. the individual $n_m(T)$ curves are shifted to lower temperature as the cooling rate increases. This analysis supports the interpretation of a time dependence of ice nucleation induced by the two Class A and Class C Snomax® IN. Therefore, we may analyze the data shown in Fig. 6a with the stochastic approach by determining the nucleation rate $R(T)$. When droplets are cooled at a constant cooling rate β and temperature is divided into equally spaced intervals (see above), the nucleation rate $R(T)$ at the interval temperature T can be derived from the number of

AMTD
7, 9137–9172, 2014

droplets nucleated in that interval $\Delta n_{ice}(T)$ (Koop et al., 1997; Zobrist et al., 2007):

$$R(T) = \frac{\Delta n_{ice}(T)}{t_{tot}(T)} \tag{3}$$

$$= \frac{\Delta n_{ice}(T) \cdot \beta}{\Delta T \cdot \left(n_{liq}(T_1) - \Delta n_{ice}(T)\right) + \sum_{j=1}^{\Delta n_{ice}(T)} (T_1 - T_{nuc,j})} \tag{4}$$

$$\approx \frac{\Delta n_{ice}(T) \cdot \beta}{\Delta T \cdot \left(n_{liq}(T_1) - 0.5 \cdot \Delta n_{ice}(T)\right)}, \tag{5}$$

where $j = 1, \ldots, \Delta n_{ice}(T)$ are the nucleation events in individual droplets occurring at temperature $T_{nuc,j}$ within the interval ΔT.

Figure 6b shows $R(T)$ determined in this way for both Classes of IN. Now the data points obtained from the different cooling rates converge onto a single line, with data obtained at larger cooling rate (yellow) representing larger values of R than those obtained at lower cooling rate (blue). These data of $R(T)$ can be normalized to the total surface area per droplet A, which for the case of a single-component (sc) ice nucleator is equivalent to nucleation rate coefficient $j_{het}(T)$,

$$\frac{R(T)}{A} = \frac{R(T)}{S' C_m V} \overset{sc}{=} j_{het}(T), \tag{6}$$

with the parameters S', C_m, and V as defined above. The value of the specific surface area S' of Snomax® was derived as follows. For the specific particle number of cells in Snomax® we used the value determined by Wex et al. (2014), see the calculation of $n_n(T)$ above. Furthermore, Wex et al. (2014) investigated the size of the particles/cells suspended in freshly prepared Snomax® suspensions by dynamic light scattering, resulting in a mean equivalent hydrodynamic radius of $r_h = 0.5\,\mu m$. Accordingly, we assumed that each cell has a surface area equivalent to that of a sphere with a radius of 0.5 µm, i.e. a surface area of $3.14\,\mu m^2$ per cell. These numbers result in

AMTD
7, 9137–9172, 2014

a value of $S' = 44\,\mathrm{cm}^2\,\mathrm{mg}^{-1}$, which was used here. The results of the analysis according to Eq. (6) are the data points plotted in Fig. 6c, which shows that $R(T)/A$ increases by about 3 orders of magnitude for a reduction in temperature of about 2 K for Class C (circles) and by about 4 orders of magnitude for a reduction of about 1 K for Class A (triangles).

The lines in Fig. 6c are fits to these data using the framework of classical nucleation theory (CNT), in which $j_{\mathrm{het}}(T,\alpha)$ can be derived (Pruppacher and Klett, 1997):

$$j_{\mathrm{het}}(T,\alpha) = \frac{kT}{h}\exp\left(-\frac{\Delta F_{\mathrm{diff}}(T)}{kT}\right) n\cdot\exp\left(-\frac{\Delta G(T)\varphi(\alpha)}{kT}\right). \quad (7)$$

Here k is the Boltzmann constant and h is the Planck constant, T is absolute temperature, and n is the number density of water molecules at the IN/water interface. $\Delta F_{\mathrm{diff}}(T)$ and $\Delta G(T)$ are the diffusion activation energy of a water molecule crossing the water/ice embryo interface and the Gibbs free energy for critical ice embryo formation without the presence of a heterogeneous IN, respectively. In the presence of an ice nucleus $\Delta G(T)$ is modified by the compatibility function $\varphi(\alpha)$:

$$\varphi(\alpha) = \frac{1}{4}(2+\cos\,\alpha)(1-\cos\,\alpha)^2, \quad (8)$$

where the parameter α represents a hypothetical effective contact angle between the forming ice embryo and the IN in water, which can vary between 0 and 180°. An effective contact angle of $\alpha = 0°$ implies a perfect IN leading to $\varphi = 0$ and a negligible Gibbs free energy term (equivalent to seeding by a mother crystal). An effective contact angle of $\alpha = 180°$ leads to $\varphi = 1$ and the Gibbs free energy term is not reduced, implying a maximally poor IN and, thus, nucleation occurs at the rate of homogeneous ice nucleation. For our analysis we use α as the only free parameter in a fit of CNT to the data. Temperature-dependant parameterizations for all other quantities were obtained from Zobrist et al. (2007). Figure 6c shows that the measured data are not well described by CNT when using constant effective contact angle values of $\alpha = 23.9°$ and

AMTD
7, 9137–9172, 2014

$\alpha = 35.3^{\circ}$ for Class A and C, respectively (gray lines). Allowing for a linear temperature dependence of α, a much better fit of CNT to the data results (red and blue lines). The corresponding linear equations for the temperature-dependent effective contact angles are $\alpha(T) = 613.5 - 2.188 \cdot T$ and $\alpha(T) = 286.5 - 0.9495 \cdot T$ for Class A and C, respectively. (Note that the input temperatures are in the unit of kelvins.) To further emphasize the effect of the steep increase of $j_{het}(T)$ with decreasing temperature found for both IN Classes the parameterizations were also used to calculate the nucleation probability P_{i0} as a function of temperature and observation time (see Fig. 9 in the Appendix). We found that changing observation time by several orders of magnitude results in a change of P_{i0} from zero to one in a narrow temperature range smaller than 1 K. In contrast, at a constant temperature the same change in P_{i0} requires a difference in observation time of more than one order of magnitude.

It is interesting to compare the magnitude of time dependence of Snomax® with that of other IN of atmospheric relevance. In a very recent study Herbert et al. (2014) proposed the following equation for the description of cooling rate dependence of a single IN (applied to $T_{f,50}$ values here):

$$T_{f,50}(\beta_2) - T_{f,50}(\beta_1) = \Delta T_{f,50} = \frac{1}{\lambda} \cdot \ln\left(\frac{\beta_1}{\beta_2}\right). \quad (9)$$

Here, $T_{f,50}(\beta_2)$ and $T_{f,50}(\beta_1)$ are the median freezing temperatures at cooling rates β_2 and β_1, respectively, and λ is a constant. Herbert et al. (2014) point out that for a single-component IN following stochastic (i.e. non-singular) behavior λ is the temperature dependence of the heterogeneous ice nucleation rate coefficient of the IN: $\lambda = -\mathrm{d}\ln(j_{het})/\mathrm{d}T$. We note that an equation similar to Eq. (9) was originally introduced by Vali and Stansbury (1966) for the mean freezing temperature, i.e. $\overline{T}_f(\beta_2) - \overline{T}_f(\beta_1) = \xi \cdot \ln\left(\frac{\beta_1}{\beta_2}\right)$. Ignoring any difference between $\overline{T}_f$ and $T_{f,50}$ (which occurs, e.g., for a T_f distribution that is constant with changing cooling rate) implies that the constant ξ is related to λ via $\xi = \lambda^{-1}$. For the singular case $\xi_{si} = 0$ and $\lambda_{si} = \infty$ by definition, and a small ξ/large λ value indicates a behavior that is close to singular, i.e. nucleation

AMTD
7, 9137–9172, 2014

shows a less-pronounced stochastic time dependence. Moreover, one can define the temperature dependence of the normalized freezing rate $\omega = -\mathrm{d}\ln(R/A)/\mathrm{d}T$ and note that $\omega = \lambda$ for a single-component IN and $\omega < \lambda$ for a multi-component IN (Vali, 2014; Herbert et al., 2014).

Using Eq. (9) with the $T_{\mathrm{f},50}$ data shown in Fig. 5 at minimal ($0.1\,\mathrm{K\,min^{-1}}$) and maximal ($10\,\mathrm{K\,min^{-1}}$) cooling rate yields a value of $\lambda = 8.4 \pm 2.3\,\mathrm{K^{-1}}$ for the Class A IN and $\lambda = 7.2 \pm 3.2\,\mathrm{K^{-1}}$ for class C IN, respectively (magenta triangles in Fig. 7). Similarly, we can linearly fit the data shown in Fig. 5 and derive λ from the slopes of these lines as $\lambda = 8.5 \pm 1.4\,\mathrm{K^{-1}}$ and $\lambda = 7.6 \pm 0.9\,\mathrm{K^{-1}}$ (orange circles in Fig. 7). We note that the two different ways for deriving λ agree well with each other. Moreover, we can also determine ω from the data shown in Fig. 6c. Fitting a straight line to $\ln(R(T)/A)$ vs. T data results in $\omega = 8.7 \pm 0.4\,\mathrm{K^{-1}}$ for the Class A IN and $\omega = 5.4 \pm 0.2\,\mathrm{K^{-1}}$ for class C IN, respectively (green diamonds in Fig. 7).

The non-linear behavior of the $R(T)/A$ data in the logarithmic plot of Fig. 6c suggest that λ is not constant, but instead shows a temperature dependence itself. For these reasons we finally derive λ by taking the derivative of the CNT fit to the data (solid lines in Fig. 6c), i.e. $\lambda = -\mathrm{d}\ln(j_{\mathrm{het}})/\mathrm{d}T$ resulting in the red and blue lines for $\lambda(T)$ over the investigated temperature range (Fig. 7). Clearly, the ω-value is consistent with the $\lambda(T)$-value in that it represents an average value over the investigated temperature range. However, the particularly strong difference between ω and λ obtained for the Class C IN and the fact $\omega < \lambda$ that may be indicative of the fact that Class C IN consist of a multi-component set of IN (see discussion in Herbert et al., 2014). In contrast, the good agreement between ω and λ obtained for the Class A IN suggest that these are indeed single-component IN and, hence, $\omega = \lambda$ in this case.

The λ-values derived here can be compared to values for other types of IN from the literature. For example, the values for various mineral dusts (ATD, illite NX, kaolinite KG-1b, and feldspar) range between about $1\,\mathrm{K^{-1}}$ and $4.5\,\mathrm{K^{-1}}$ (Murray et al., 2011; Wright and Petters, 2013; Hiranuma et al., 2013; Vali, 2014; Herbert et al., 2014). Furthermore, the literature analysis of λ-values by Herbert et al. (2014) includes also other types of

AMTD
7, 9137–9172, 2014

IN. This comparison indicates the smallest value of $\lambda = 0.6\,K^{-1}$ for volcanic ash (Fornea et al., 2009; Hoyle et al., 2011; Steinke et al., 2011), and the highest value of $\lambda = 6.3\,K^{-1}$ for a soil sample (Vali, 2008). When we use homogeneous ice nucleation data in pure water at temperatures between about −38 °C (235 K) and −35 °C (238 K) a mean value of $\lambda = 3.4 \pm 1.2\,K^{-1}$ results (Riechers et al., 2013). The rather small λ-values for most IN compounds emphasize the stochastic nature of heterogenous ice nucleation in these cases. They also indicate that the values obtained here for Snomax® are even larger than that of homogeneous ice nucleation implying a very small "stochasticity" of the responsible IN moieties. To our knowledge the value of $\lambda = 8.7\,K^{-1}$ for the Class A IN of Snomax® obtained here is the largest λ-value reported to date, emphasizing the capability of the apparatus introduced here. Moreover, since we were able to detect such a large λ-value suggests that the BINARY setup is suitable for measuring time dependence for most other IN of atmospheric interest, making it a useful tool for future analysis.

5 Conclusions

Herein we introduced the novel optical freezing array BINARY for studying the temperature and time dependence of heterogeneous ice nucleation in the immersion mode. The principal advantages of the technique is prevention of a Wegener–Bergeron–Findeisen type water vapor transfer between unfrozen and frozen droplets and of a seeding of neighboring droplets by formation and surface growth of frost halos. The simultaneous study of 36 droplets and a fully automated evaluation of the ice nucleation temperature in each droplet from a real time image analysis allows for a facile and fast accumulation of data points. Moreover, the microliter volume of the investigated droplets permits a preparation of droplets with IN concentrations varying over several orders of magnitude thus enabling the detection of rare ice nucleators of high activity. The BINARY setup was tested by studying heterogeneous ice nucleation induced by Snomax® sus-

AMTD
7, 9137–9172, 2014

pended in water droplets at various concentrations from 1 ng mL^{-1} to 1 mg mL^{-1}. Two types of IN were clearly identified, namely Class A and Class C ice nucleators. Using different cooling rates we were able to show that these IN exhibit a minute time dependence which we quantified by analyzing the experimental data in terms of the temperature dependence of the ice nucleation rate coefficient $\lambda = -\mathrm{d}\ln(j_{\mathrm{het}}(T))/\mathrm{d}T$. While Class C Snomax® IN appear to be multi-component, the data for Class A are consistent with a single-component IN. To the best of our knowledge, the resulting $\lambda = 8.7\,\mathrm{K}^{-1}$ for the Class A Snomax® IN is the largest λ-value reported to date, thus highlighting the capability of the BINARY device.

Appendix A: Additional information and data analysis

A1 Calibration literature values

For the temperature calibration described in Sect. 3 information about the literature values of the phase transitions of the reference substances were required. Most of the values are taken from Linstrom and Mallard (2014) and publications cited therein. Data which was excluded from the overall average by NIST was also excluded here. In addition to the NIST data, values were taken from Parks and Huffman (1931); Messerly et al. (1967) and Mondieig et al. (2004). Figure 8 shows an overview of all data used here. A summary of the particular phase transitions and the median literature values are given in Table 1.

A2 Ice nucleation probability

The CNT parameterizations with a temperature-dependent $\alpha(T)$ shown as red and blue lines in Fig. 6c were used to calculate the ice nucleation probability P_{i0} as a function of

AMTD
7, 9137–9172, 2014

time and temperature for typical experimental conditions. Here

$$P_{i0}(T,\Delta t) = \frac{\Delta n_{\mathrm{ice}}(T,\Delta t)}{n_{\mathrm{liq}}(T,t_1)} = 1 - e^{-R(T)\Delta t} \quad \text{(A1)}$$

represents the number of frozen droplets $\Delta n_{\mathrm{ice}}(T,\Delta t) = n_{\mathrm{liq}}(T,t_1) - n_{\mathrm{liq}}(T,t_2)$ at constant temperature T in a time interval $\Delta t = t_2 - t_1$. Figure 9 shows the results for 1 microliter droplets containing Snomax® at 1×10^{-1} µg drop^{-1} (Class A) in the top panel (a) and for droplets containing Snomax® at 1×10^{-5} µg drop^{-1} (Class C) in the bottom panel (b). The contour plots indicate very abrupt changes of the nucleation probabilities from zero to one with decreasing temperature for both Classes of IN. The corresponding temperature interval in which the transition occurs is smaller than about 0.5 K for time intervals of 0.1 s for Class C IN. An even smaller temperature interval of about 0.2 K results for larger time intervals and Class A IN at 1×10^{-1} µg drop^{-1}. Figure 9 reinforces our interpretation provided in the results section that also the ice nucleation probability of Snomax® IN shows a very strong temperature dependence but only a rather small time dependence.

The Supplement related to this article is available online at doi:10.5194/amtd-7-9137-2014-supplement.

Acknowledgements. The authors gratefully acknowledge funding by the German Research Foundation (DFG) through the research unit INUIT (FOR 1525) under KO 2944/2-1. We particularly thank our INUIT partners for fruitful collaboration and sharing of ideas and IN samples. We also thank K. Dreischmeier and D. Cherian for testing and discussing features of the BINARY setup, and R. Herbert and B. Murray for helpful discussions on λ-analysis.

AMTD
7, 9137–9172, 2014

References

Atkinson, J. D., Murray, B. J., Woodhouse, M. T., Whale, T. F., Baustian, K. J., Carslaw, K. S., Dobbie, S., O'Sullivan, D., and Malkin, T. L.: The importance of feldspar for ice nucleation by mineral dust in mixed-phase clouds, Nature, 498, 355–358, doi:10.1038/nature12278, 2013. 9141

Attard, E., Yang, H., Delort, A.-M., Amato, P., Pöschl, U., Glaux, C., Koop, T., and Morris, C. E.: Effects of atmospheric conditions on ice nucleation activity of *Pseudomonas*, Atmos. Chem. Phys., 12, 10667–10677, doi:10.5194/acp-12-10667-2012, 2012. 9141

Barlow, T. W. and Haymet, A. D. J.: ALTA: An automated lag-time apparatus for studying the nucleation of supercooled liquids, Rev. Sci. Instrum., 66, 2996, doi:10.1063/1.1145586, 1995. 9141

Bigg, E. K.: The supercooling of water, Proc. Phys. Soc. Sect. B, 66, 688–694, doi:10.1088/0370-1301/66/8/309, 1953. 9139, 9140

Connolly, P. J., Möhler, O., Field, P. R., Saathoff, H., Burgess, R., Choularton, T., and Gallagher, M.: Studies of heterogeneous freezing by three different desert dust samples, Atmos. Chem. Phys., 9, 2805–2824, doi:10.5194/acp-9-2805-2009, 2009. 9147

Cziczo, D. J. and Froyd, K. D.: Sampling the composition of cirrus ice residuals, Atmos. Res., 142, 15–31, doi:10.1016/j.atmosres.2013.06.012, 2014. 9138

Della Gatta, G., Richardson, M. J., Sarge, S. M., and Stølen, S.: Standards, calibration, and guidelines in microcalorimetry. Part 2. Calibration standards for differential scanning calorimetry (IUPAC Technical Report), Pure Appl. Chem., 78, 1455–1476, doi:10.1351/pac200678071455, 2006. 9145, 9146

Ervens, B. and Feingold, G.: Sensitivities of immersion freezing: reconciling classical nucleation theory and deterministic expressions, Geophys. Res. Lett., 40, 3320–3324, doi:10.1002/grl.50580, 2013. 9139

Fletcher, N. H.: Active sites and ice crystal nucleation, J. Atmos. Sci., 26, 1266–1271, doi:10.1175/1520-0469(1969)026<1266:ASAICN>2.0.CO;2, 1969. 9147

Fornea, A. P., Brooks, S. D., Dooley, J. B., and Saha, A.: Heterogeneous freezing of ice on atmospheric aerosols containing ash, soot, and soil, J. Geophys. Res., 114, D13 201, doi:10.1029/2009JD011958, 2009. 9154

AMTD
7, 9137–9172, 2014

Hartmann, S., Augustin, S., Clauss, T., Wex, H., Šantl-Temkiv, T., Voigtländer, J., Niedermeier, D., and Stratmann, F.: Immersion freezing of ice nucleation active protein complexes, Atmos. Chem. Phys., 13, 5751–5766, doi:10.5194/acp-13-5751-2013, 2013. 9148

Heneghan, A. F., Wilson, P. W., and Haymet, A. D. J.: Heterogeneous nucleation of supercooled water, and the effect of an added catalyst., Proc. Natl. Acad. Sci. USA, 99, 9631–9634, doi:10.1073/pnas.152253399, 2002. 9141

Herbert, R. J., Murray, B. J., Whale, T. F., Dobbie, S. J., and Atkinson, J. D.: Representing time-dependent freezing behaviour in immersion mode ice nucleation, Atmos. Chem. Phys., 14, 8501–8520, doi:10.5194/acp-14-8501-2014, 2014. 9145, 9152, 9153

Hiranuma, N., Möhler, O., Bingemer, H., Bundke, U., Cziczo, D. J., Danielczok, A., Ebert, M., Garimella, S., Hoffmann, N., Höhler, K., Kanji, Z. A., Kiselev, A., Raddatz, M., and Stetzer, O.: Immersion freezing of clay minerals and bacterial ice nuclei, in: Nucleation Atmos. Aerosols (AIP Conf. Proc. 1527), edited by DeMott, P. J. and O'Dowd, C. D., 914–917, doi:10.1063/1.4803420, AIP Publishing, Melville, NY, USA, 2013. 9153

Hoffer, T. E.: A laboratory investigation of droplet freezing, J. Meteorol., 18, 766–778, doi:10.1175/1520-0469(1961)018<0766:ALIODF>2.0.CO;2, 1961. 9140

Hoose, C. and Möhler, O.: Heterogeneous ice nucleation on atmospheric aerosols: a review of results from laboratory experiments, Atmos. Chem. Phys., 12, 9817–9854, doi:10.5194/acp-12-9817-2012, 2012. 9139, 9140

Hoyle, C. R., Pinti, V., Welti, A., Zobrist, B., Marcolli, C., Luo, B., Höskuldsson, Á., Mattsson, H. B., Stetzer, O., Thorsteinsson, T., Larsen, G., and Peter, T.: Ice nucleation properties of volcanic ash from Eyjafjallajökull, Atmos. Chem. Phys., 11, 9911–9926, doi:10.5194/acp-11-9911-2011, 2011. 9154

Iannone, R., Chernoff, D. I., Pringle, A., Martin, S. T., and Bertram, A. K.: The ice nucleation ability of one of the most abundant types of fungal spores found in the atmosphere, Atmos. Chem. Phys., 11, 1191–1201, doi:10.5194/acp-11-1191-2011, 2011. 9141

Jung, S., Tiwari, M. K., and Poulikakos, D.: Frost halos from supercooled water droplets., Proc. Natl. Acad. Sci. USA, 109, 16073–16078, doi:10.1073/pnas.1206121109, 2012. 9140

Knopf, D. A. and Lopez, M. D.: Homogeneous ice freezing temperatures and ice nucleation rates of aqueous ammonium sulfate and aqueous levoglucosan particles for relevant atmospheric conditions, Phys. Chem. Chem. Phys., 11, 8056–8068, doi:10.1039/b903750k, 2009. 9141

AMTD
7, 9137–9172, 2014

Koop, T. and Zobrist, B.: Parameterizations for ice nucleation in biological and atmospheric systems., Phys. Chem. Chem. Phys., 11, 10839–10850, doi:10.1039/b914289d, 2009. 9141
Koop, T., Luo, B., Biermann, U. M., Crutzen, P. J., and Peter, T.: Freezing of $HNO_3/H_2SO_4/H_2O$ solutions at stratospheric temperatures: nucleation statistics and experiments, J. Phys. Chem. A, 101, 1117–1133, doi:10.1021/jp9626531, 1997. 9150
Koop, T., Ng, H. P., Molina, L. T., and Molina, M. J.: A new optical technique to study aerosol phase transitions: the nucleation of ice from H_2SO_4 aerosols, J. Phys. Chem. A, 102, 8924–8931, doi:10.1021/jp9828078, 1998. 9141
Koop, T., Kapilashrami, A., Molina, L. T., and Molina, M. J.: Phase transitions of sea-salt/water mixtures at low temperatures: implications for ozone chemistry in the polar marine boundary layer, J. Geophys. Res., 105, 26393, doi:10.1029/2000JD900413, 2000. 9138
Kulkarni, G., Fan, J., Comstock, J. M., Liu, X., and Ovchinnikov, M.: Laboratory measurements and model sensitivity studies of dust deposition ice nucleation, Atmos. Chem. Phys., 12, 7295–7308, doi:10.5194/acp-12-7295-2012, 2012. 9139
Lamb, D. and Verlinde, J.: Physics and Chemistry of Clouds, Cambridge University Press, Cambridge, doi:10.1017/CBO9780511976377, 2011. 9138
Linstrom, P. J. and Mallard, W. G. (Eds.): NIST Chemistry WebBook, NIST Standard Reference Database Number 69, National Institute of Standards and Technology, Gaithersburg MD, 20899, available at: http://webbook.nist.gov, last access: 8 September 2014. 9155
Lohmann, U. and Diehl, K.: Sensitivity studies of the importance of dust ice nuclei for the indirect aerosol effect on stratiform mixed-phase clouds, J. Atmos. Sci., 63, 968–982, doi:10.1175/JAS3662.1, 2006. 9139
Lüönd, F., Stetzer, O., Welti, A., and Lohmann, U.: Experimental study on the ice nucleation ability of size-selected kaolinite particles in the immersion mode, J. Geophys. Res., 115, D14201, doi:10.1029/2009JD012959, 2010. 9140
Messerly, J. F., Guthrie, G. B., Todd, S. S., and Finke, H. L.: Low-temperature thermal data for pentane, n-heptadecane, and n-octadecane. Revised thermodynamic functions for the n-alkanes, C5–C18, J. Chem. Eng. Data, 12, 338–346, doi:10.1021/je60034a014, 1967. 9155
Mondieig, D., Rajabalee, F., Metivaud, V., Oonk, H. A. J., and Cuevas-Diarte, M. A.: n-alkane binary molecular alloys, Chem. Mater., 16, 786–798, doi:10.1021/cm031169p, 2004. 9155
Murphy, D. M. and Koop, T.: Review of the vapour pressures of ice and supercooled water for atmospheric applications, Q. J. Roy. Meteor. Soc., 131, 1539–1565, doi:10.1256/qj.04.94, 2005. 9142

AMTD
7, 9137–9172, 2014

Murray, B. J., Broadley, S. L., Wilson, T. W., Bull, S. J., Wills, R. H., Christenson, H. K., and Murray, E. J.: Kinetics of the homogeneous freezing of water., Phys. Chem. Chem. Phys., 12, 10380–10387, doi:10.1039/c003297b, 2010. 9139, 9141

Murray, B. J., Broadley, S. L., Wilson, T. W., Atkinson, J. D., and Wills, R. H.: Heterogeneous freezing of water droplets containing kaolinite particles, Atmos. Chem. Phys., 11, 4191–4207, doi:10.5194/acp-11-4191-2011, 2011. 9140, 9141, 9153

Murray, B. J., O'Sullivan, D., Atkinson, J. D., and Webb, M. E.: Ice nucleation by particles immersed in supercooled cloud droplets., Chem. Soc. Rev., 41, 6519–6554, doi:10.1039/c2cs35200a, 2012. 9140, 9147

Niedermeier, D., Hartmann, S., Shaw, R. A., Covert, D., Mentel, T. F., Schneider, J., Poulain, L., Reitz, P., Spindler, C., Clauss, T., Kiselev, A., Hallbauer, E., Wex, H., Mildenberger, K., and Stratmann, F.: Heterogeneous freezing of droplets with immersed mineral dust particles – measurements and parameterization, Atmos. Chem. Phys., 10, 3601–3614, doi:10.5194/acp-10-3601-2010, 2010. 9140

Niemand, M., Möhler, O., Vogel, B., Vogel, H., Hoose, C., Connolly, P., Klein, H., Bingemer, H., DeMott, P., Skrotzki, J., and Leisner, T.: A particle-surface-area-based parameterization of immersion freezing on desert dust particles, J. Atmos. Sci., 69, 3077–3092, doi:10.1175/JAS-D-11-0249.1, 2012. 9147

O'Sullivan, D., Murray, B. J., Malkin, T. L., Whale, T. F., Umo, N. S., Atkinson, J. D., Price, H. C., Baustian, K. J., Browse, J., and Webb, M. E.: Ice nucleation by fertile soil dusts: relative importance of mineral and biogenic components, Atmos. Chem. Phys., 14, 1853–1867, doi:10.5194/acp-14-1853-2014, 2014. 9142

Parks, G. S. and Huffman, H. M.: Some fusion and transition data for hydrocarbons, Ind. Eng. Chem., 23, 1138–1139, doi:10.1021/ie50262a018, 1931. 9155

Pruppacher, H. R. and Klett, J. D.: Microphysics of Clouds and Precipitation, 2 edn., Kluwer Academic Publishers, New York, 1997. 9138, 9139, 9151

Pummer, B. G., Bauer, H., Bernardi, J., Bleicher, S., and Grothe, H.: Suspendable macromolecules are responsible for ice nucleation activity of birch and conifer pollen, Atmos. Chem. Phys., 12, 2541–2550, doi:10.5194/acp-12-2541-2012, 2012. 9140, 9141

Riechers, B., Wittbracht, F., Hütten, A., and Koop, T.: The homogeneous ice nucleation rate of water droplets produced in a microfluidic device and the role of temperature uncertainty, Phys. Chem. Chem. Phys., 15, 5873–5887, doi:10.1039/c3cp42437e, 2013. 9139, 9146, 9154

AMTD
7, 9137–9172, 2014

Salcedo, D., Molina, L. T., and Molina, M. J.: Nucleation rates of nitric acid dihydrate in 1 : 2 HNO_3/H_2O solutions at stratospheric temperatures, Geophys. Res. Lett., 27, 193, doi:10.1029/1999GL010991, 2000. 9141

Sarge, S. M., Höhne, G. W., Cammenga, H. K., Eysel, W., and Gmelin, E.: Temperature, heat and heat flow rate calibration of scanning calorimeters in the cooling mode, Thermochim. Acta, 361, 1–20, doi:10.1016/S0040-6031(00)00543-8, 2000. 9145, 9146

Steinke, I., Möhler, O., Kiselev, A., Niemand, M., Saathoff, H., Schnaiter, M., Skrotzki, J., Hoose, C., and Leisner, T.: Ice nucleation properties of fine ash particles from the Eyjafjallajökull eruption in April 2010, Atmos. Chem. Phys., 11, 12945–12958, doi:10.5194/acp-11-12945-2011, 2011. 9154

Stopelli, E., Conen, F., Zimmermann, L., Alewell, C., and Morris, C. E.: Freezing nucleation apparatus puts new slant on study of biological ice nucleators in precipitation, Atmos. Meas. Tech., 7, 129–134, doi:10.5194/amt-7-129-2014, 2014. 9141, 9142

Turner, M. A., Arellano, F., and Kozloff, L. M.: Three separate classes of bacterial ice nucleation structures., J. Bacteriol., 172, 2521–2526, 1990. 9148, 9167

Vali, G.: Supercooling of water and nucleation of ice (drop freezer), Am. J. Phys., 39, 1125–1128, doi:10.1119/1.1976585, 1971. 9140

Vali, G.: Freezing rate due to heterogeneous nucleation, J. Atmos. Sci., 51, 1843–1856, doi:10.1175/1520-0469(1994)051<1843:FRDTHN>2.0.CO;2, 1994. 9139

Vali, G.: Repeatability and randomness in heterogeneous freezing nucleation, Atmos. Chem. Phys., 8, 5017–5031, doi:10.5194/acp-8-5017-2008, 2008. 9139, 9154

Vali, G.: Interpretation of freezing nucleation experiments: singular and stochastic; sites and surfaces, Atmos. Chem. Phys., 14, 5271–5294, doi:10.5194/acp-14-5271-2014, 2014. 9139, 9153

Vali, G. and Stansbury, E. J.: Time-dependet characteristics of the heterogeneous nucleation of ice, Can. J. Phys., 44, 477–502, doi:10.1139/p66-044, 1966. 9139, 9140, 9141, 9152

Vonnegut, B. and Baldwin, M.: Repeated nucleation of a supercooled water sample that contains silver iodide particles, J. Clim. Appl. Meteorol., 23, 486–490, doi:10.1175/1520-0450(1984)023<0486:RNOASW>2.0.CO;2, 1984. 9139

Welti, A., Lüönd, F., Kanji, Z. A., Stetzer, O., and Lohmann, U.: Time dependence of immersion freezing: an experimental study on size selected kaolinite particles, Atmos. Chem. Phys., 12, 9893–9907, doi:10.5194/acp-12-9893-2012, 2012. 9139

AMTD
7, 9137–9172, 2014

Welz, T.: Untersuchung der Eisnukleation in wässrigen Birkenpollensuspensionen, Ba thesis, Bielefeld University, Bielefeld, 2013. 9140, 9142

Wex, H., Augustin, S., Boose, Y., Budke, C., Curtius, J., Diehl, K., Dreyer, A., Frank, F., Hartmann, S., Hiranuma, N., Jantsch, E., Kanji, Z. A., Kiselev, A., Koop, T., Möhler, O., Niedermeier, D., Nillius, B., Rösch, M., Rose, D., Steinke, I., and Stratmann, F.: Intercomparing different devices for the investigation of ice nucleating particles using Snomax as test substance, Atmos. Chem. Phys. Discuss., 14, 22321-22384, doi:10.5194/acpd-14-22321-2014, 2014. 9148, 9150

Wright, T. P. and Petters, M. D.: The role of time in heterogeneous freezing nucleation, J. Geophys. Res. Atmos., 118, 3731–3743, doi:10.1002/jgrd.50365, 2013. 9139, 9140, 9141, 9153

Yankofsky, S. A., Levin, Z., Bertold, T., and Sandlerman, N.: Some basic characteristics of bacterial freezing nuclei, J. Appl. Meteorol., 20, 1013–1019, doi:10.1175/1520-0450(1981)020<1013:SBCOBF>2.0.CO;2, 1981. 9148

Zobrist, B., Koop, T., Luo, B., Marcolli, C., and Peter, T.: Heterogeneous ice nucleation rate coefficient of water droplets coated by a nonadecanol monolayer, J. Phys. Chem. C, 111, 2149–2155, doi:10.1021/jp066080w, 2007. 9150, 9151

AMTD
7, 9137–9172, 2014

Table 1. Substances and their median phase transition temperatures derived from several sources which were used in the calibration of the BINARY setup. The errors indicate the 25th and 75th percentiles.

Substance	Purity	Type of Transition	Number of Data Points	$T_{lit,50\%}$ [°C]
Water	double-distilled	solid–liquid	–	0.00
Tridecane	≥ 99.5 %	solid–liquid	20	$-5.41\ ^{+0.05}_{-0.39}$
Tridecane	≥ 99.5 %	solid–solid	3	$-18.15\ ^{+0.20}_{-0.00}$
Undecane	≥ 99.8 %	solid–liquid	26	$-25.61\ ^{+0.01}_{-0.29}$
Undecane	≥ 99.8 %	solid–solid	5	$-36.85\ ^{+0.30}_{-0.15}$

AMTD
7, 9137–9172, 2014

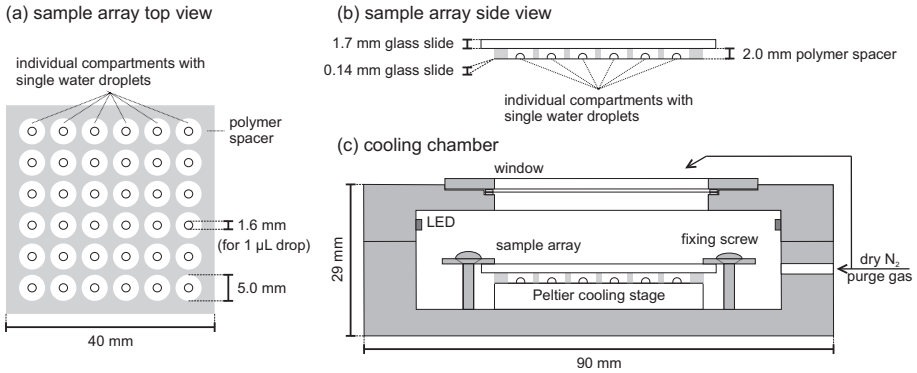

Figure 1. Schematic of the Bielefeld Ice Nucleation ARraY (BINARY) setup. **(a)** Top view of the 6×6 droplet array. The droplets are separated from each other by a polymer spacer creating individual compartments. **(b)** Side view showing the sealing of the compartments by top and bottom glass slides. **(c)** Position of the sample array on the Peltier cooling stage inside the cooling chamber.

AMTD
7, 9137–9172, 2014

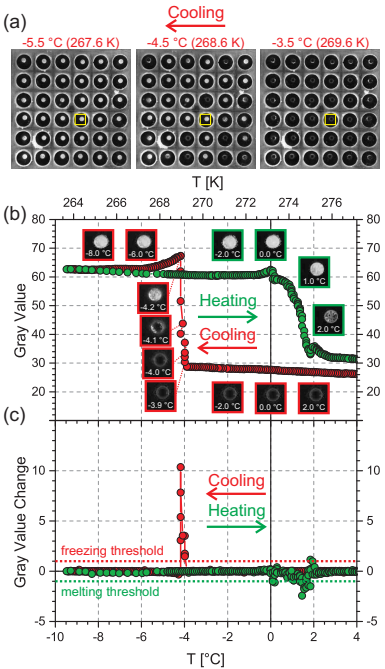

Figure 2. Example experiment with Snomax® containing droplets (1×10^{-1} µg drop^{-1}) describing the automatic detection of nucleation events by the change in brightness during freezing. A movie of this experiment is available via the Supplement. **(a)** Image series of the 6×6 droplet array during cooling. **(b)** Measured gray value of the compartment/droplet indicated by the yellow box in panel **(a)** during cooling (red) and heating (green). Freezing and melting start at −3.9 °C (269.2 K) and 0.0 °C (273.2 K), respectively. **(c)** Plot of the change in gray value between successive images showing peaks at the phase transition points. Threshold values of ±1 for the automatic attribution of freezing and melting are indicated by dashed lines.

AMTD
7, 9137–9172, 2014

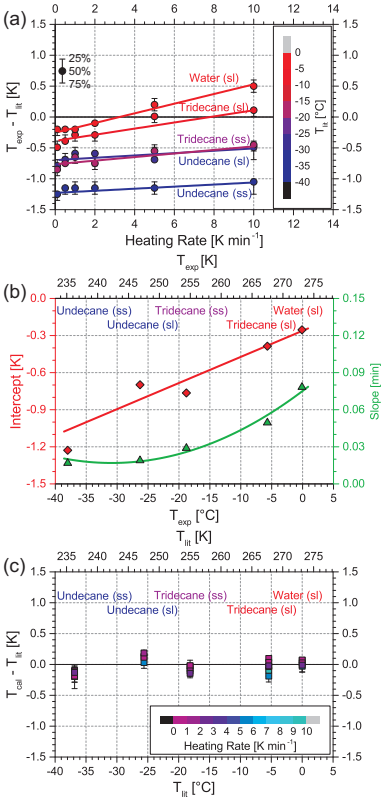

Figure 3. Temperature calibration. **(a)** Difference between the experimentally determined phase transition temperatures of water, tridecane, and undecane droplets and the corresponding literature values as a function of heating rate. Linear fits to the data are indicated by the solid lines. **(b)** Intercepts (left, red) and slopes (right, green) of the linear fits shown in panel **(a)** above. The experimentally determined data (symbols) are fitted by a linear function (intercepts, red line) and by a second-order polynomial (slopes, green line). **(c)** Residual difference between the calibrated phase transition temperatures and the literature values after calibration.

AMTD
7, 9137–9172, 2014

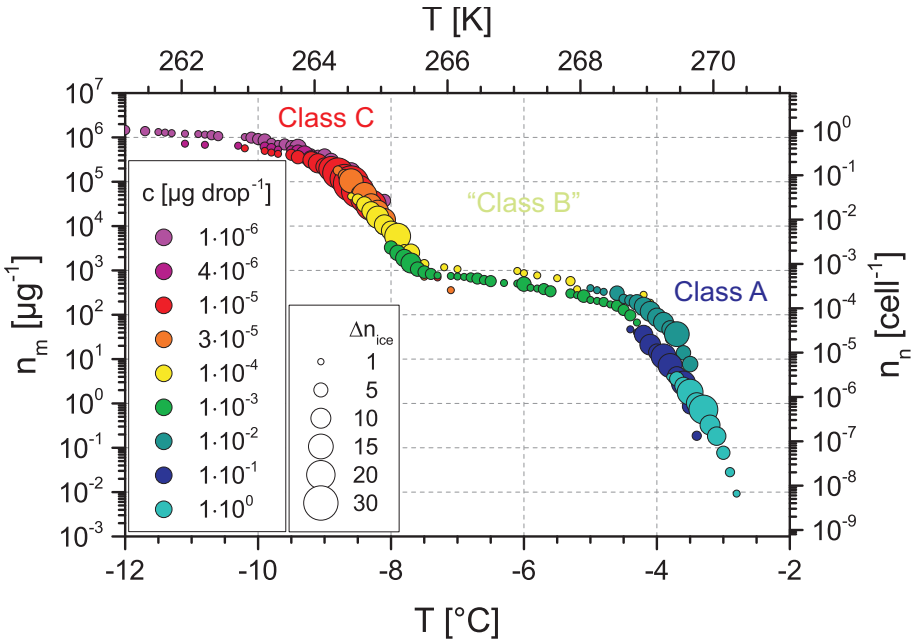

Figure 4. Experimentally determined active site density per unit mass of Snomax® $n_m(T)$ vs. temperature. Symbol colors indicate data from droplets with different Snomax® concentrations, symbol size indicates the number of nucleating droplets per temperature interval. The temperature range for different Classes of IN according to the definition by Turner et al. (1990) are also indicated.

AMTD
7, 9137–9172, 2014

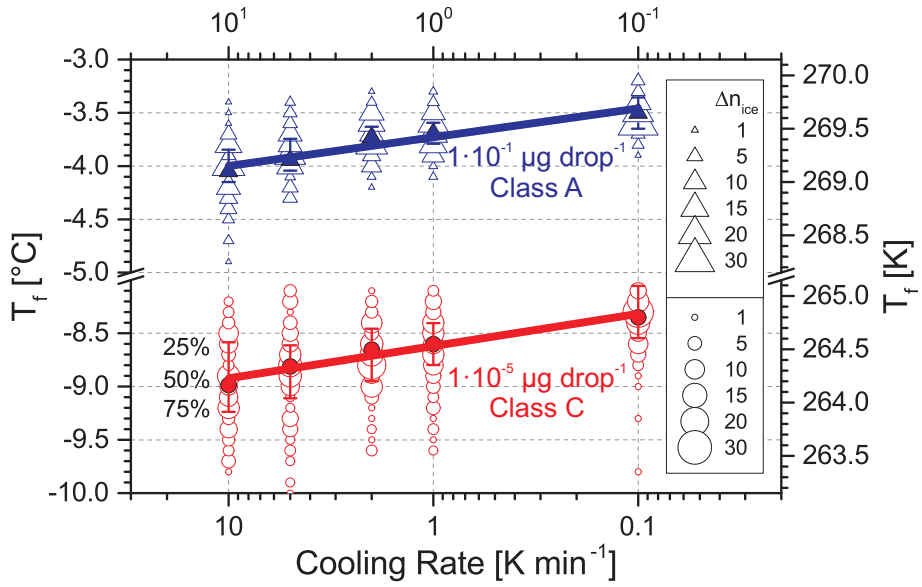

Figure 5. Freezing temperatures of water droplets containing Snomax® at concentrations of 1×10^{-5} µg drop^{-1} (red) and 1×10^{-1} µg drop^{-1} (blue) as a function of experimental cooling rate. The number of nucleation events at individual temperatures is indicated by the size of the open symbols. Solid symbols indicate the median freezing temperature ($T_{f,50}$) with error bars representing the 25th and 75th percentiles. Solid lines are linear fits to the solid symbols, see text.

AMTD
7, 9137–9172, 2014

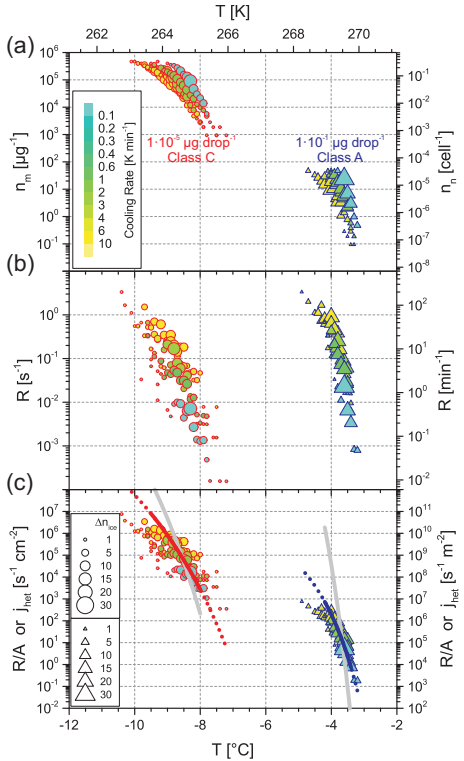

Figure 6. (a) Cooling rate dependence of the active site densities per mass ($n_m(T)$) and per cell ($n_n(T)$) vs. temperature for two Classes of IN determined from droplets containing the indicated Snomax® concentrations. **(b)** Stochastic analysis of the data from panel **(a)** in terms of the nucleation rate $R(T)$. **(c)** Normalized nucleation rate $R(T)/A$ data derived from the $R(T)$ data in panel **(b)** following Eq. (6) (data points) and analysis of these data in terms of the heterogeneous ice nucleation rate coefficient $j_{het}(T)$ using CNT with a constant effective contact angle α (gray lines) and a linear temperature dependence of α (colored lines).

AMTD
7, 9137–9172, 2014

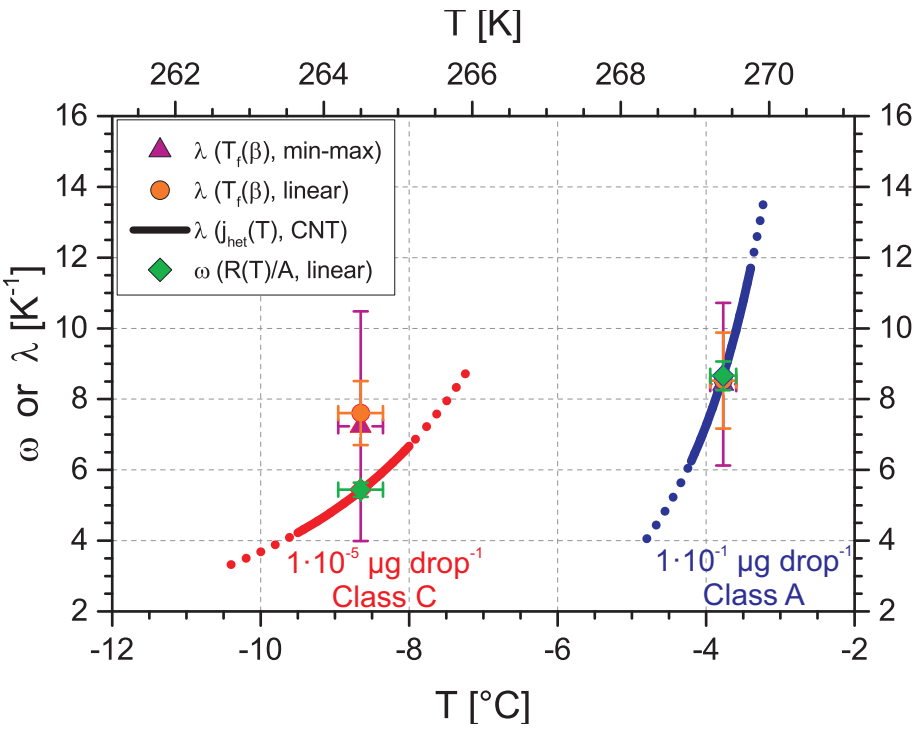

Figure 7. Value of ω and λ derived in different ways for the two indicated Classes of Snomax® IN. Magenta triangle: λ obtained from Eq. (9) at the minimal (0.1 K min^{-1}) and maximal (10 K min^{-1}) cooling rate. Orange circle: λ obtained from the linear fits to the $T_{f,50}$ data shown in Fig. 5. Green diamond: $\omega = -\mathrm{d}\ln(R/A)/\mathrm{d}T$ obtained from a linear fit to the $R(T)/A$ data shown in Fig. 6c. Lines indicate λ derived from the derivative of the nucleation rate coefficient $-\mathrm{d}\ln(j_{het})/\mathrm{d}T$ based on CNT with a temperature dependent contact angle; for details see text.

AMTD
7, 9137–9172, 2014

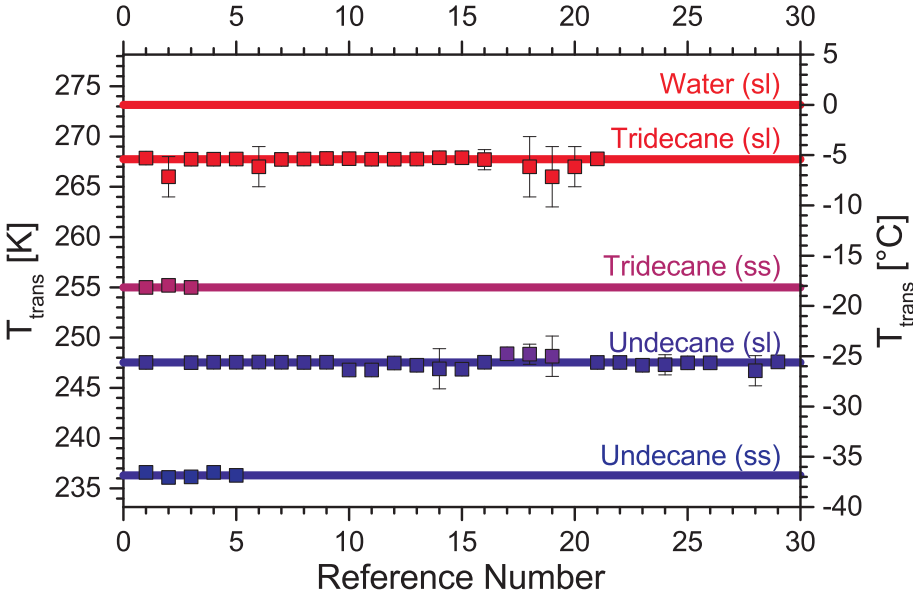

Figure 8. Literature values for the phase transitions of water, tridecane, and undecane used for the temperature calibration. Symbols indicate individual literature values and the lines represent their median used for the calibration. For data see Table 1.

AMTD
7, 9137–9172, 2014

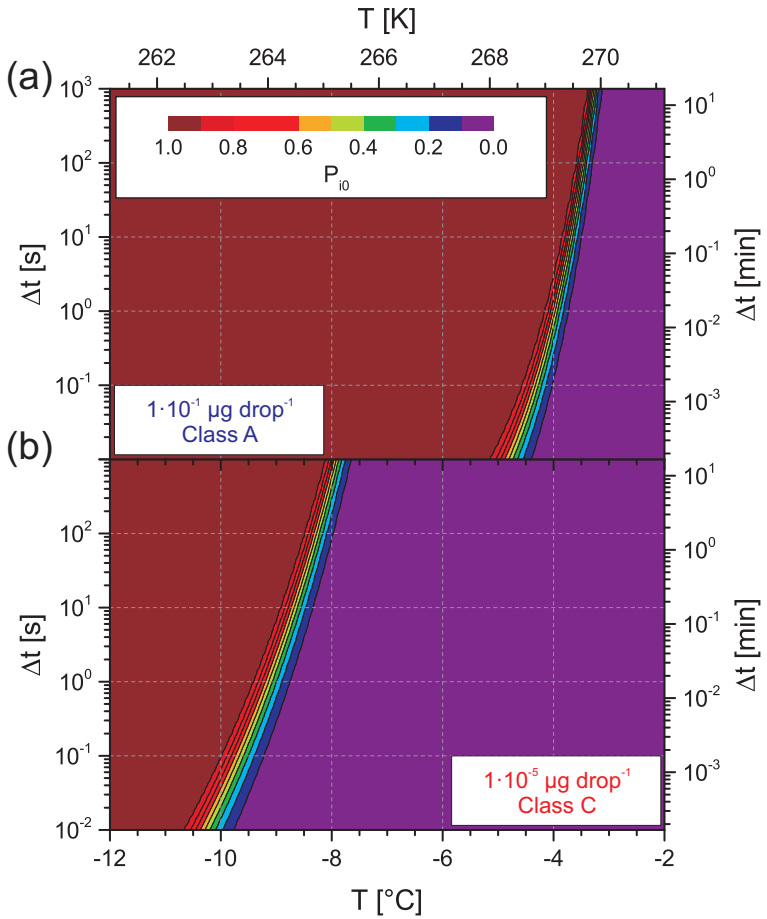

Figure 9. Contour plot of the nucleation probabilities P_{i0} as a function of time and temperature for the parametrization using CNT and temperature dependent contact angles shown in Fig. 6c for the two investigated concentrations of 1×10^{-1} µg drop^{-1} **(a)** and 1×10^{-5} µg drop^{-1} **(b)**.

AMTD
7, 9137–9172, 2014

Optical freezing array BINARY

C. Budke and T. Koop